The Astrophysical Journal Letters, 939:L23 (7pp), 2022 November 10 https://doi.org/10.3847/2041-8213/ac9b3e

Prograde and Retrograde Gas Flow around Disk-embedded Companions: Dependence on Eccentricity, Mass, and Disk Properties

Yi-Xian Chen[1], Avery Bailey[2,3], James Stone[4], and Zhaohuan Zhu[2,3]
[1] Department of Astrophysical Sciences, Princeton University, Princeton, NJ 08544, USA; yc9993@princeton.edu
[2] Department of Physics and Astronomy, University of Nevada, Las Vegas, Las Vegas, NV 89154, USA
[3] Nevada Center for Astrophysics, University of Nevada, Las Vegas, Las Vegas, NV 89154, USA
[4] School of Natural Sciences, Institute for Advanced Study, Princeton, NJ 08544, USA
Received 2022 September 18; accepted 2022 October 15; published 2022 November 9

Abstract

We apply 3D hydrodynamical simulations to study the rotational aspect of gas flow patterns around eccentric companions embedded in an accretion disk. We sample a wide range of companion mass ratios q and disk aspect ratios h_0, and confirm a generic transition from prograde (steady tidal interaction dominated) to retrograde (background Keplerian shear dominated) circumcompanion flow when orbital eccentricity exceeds a critical value e_t. We find $e_t \sim h_0$ for subthermal companions while $e_t \sim (q/h_0^3)^{1/3}$ for superthermal companions, and propose an empirical formula to unify the two scenarios. Our results also suggest that e_t is insensitive to modest levels of turbulence, modeled in the form of a kinematic viscosity term. In the context of stellar-mass black holes (sBHs) embedded in active galactic nucleus (AGN) accretion disks, the bifurcation of their circumstellar disk rotation suggests the formation of a population of nearly antialigned sBHs, whose relevance to low spin gravitational wave events can be probed in more detail with future population models of sBH evolution in AGN disks, making use of our quantitative scaling for e_t; in the context of circumplanetary disks (CPDs), our results suggest the possibility of forming retrograde satellites in situ in retrograde CPDs around eccentric planets.

Unified Astronomy Thesaurus concepts: Astrophysical black holes (98); Galaxy accretion disks (562); Protoplanetary disks (1300); Eccentricity (441)

1. Introduction

When a low-mass secondary companion is embedded in the accretion disk around its primary host, a circumcompanion disk may form within the companion's Bondi or Hills radius. In the context of protoplanetary disks (PPDs), extensive simulations establish the formation of prograde circumplanetary disks (CPDs) around embedded planets on circular orbits (Korycansky & Papaloizou 1996; Lubow et al. 1999; Tanigawa & Watanabe 2002; Machida et al. 2008; Tanigawa et al. 2012; Ormel 2013; Szulagyi et al. 2014; Fung et al. 2015; Ormel et al. 2015a, 2015b; Li et al. 2021a; Maeda et al. 2022; Szulagyi et al. 2022). That is, the circumplanetary rotation will be aligned with the global disk rotation, maintained by steady tidal perturbation and existence of horseshoe streamlines in corotation, in competition against an effectively retrograde Keplerian background shear. Recently, it is suggested in Bailey et al. (2021) and Li et al. (2022) that with moderate orbital eccentricity ($e \gtrsim h$, where h is the disk aspect ratio), the horseshoe flows are disrupted, and the background shear will dominate to produce a retrograde CPD flow. Gas accretion from a retrograde CPD can strongly influence the evolution of planetary spins through gas accretion (Batygin 2018; Ginzburg & Chiang 2020), and may also be relevant to the formation of retrograde satellites.

Moreover, it is emphasized in Li et al. (2022) that such a phenomenon is generic for stellar-mass black holes (sBHs) embedded in active galactic nucleus (AGN) accretion disks surrounding supermassive black holes (SMBHs), since it is not uncommon for these sBHs to obtain eccentricities due to birth kicks (Lousto et al. 2012) and other dynamical interactions (Zhang et al. 2014; Secunda et al. 2019, 2020). Bifurcation of spin evolution of sBHs accreting from prograde/retrograde circumstellar disks (CSDs; analogous to CPDs) produce misaligned (or nearly antialigned) sBH populations; the coalescence of which can produce low effective spin $\chi_{\rm eff}$ events consistent with most LIGO/Virgo detections (The LIGO Scientific Collaboration et al. 2021), which reinforces the idea that AGNs could be promising sites for observable sBH merger gravitational wave events (McKernan et al. 2012, 2014; Bartos et al. 2017; Stone et al. 2017; Leigh et al. 2018; Tagawa et al. 2020a, 2020b; Davies & Lin 2020; Li et al. 2021b, 2022; Li & Lai 2022). Here the effective spin parameter $\chi_{\rm eff}$ is the mass-weighted-average of the sBH (merger components) spins projected along the binary orbital angular momentum, whose distribution can help constrain compact-object merger pathways (e.g., Gerosa et al. 2018; Bavera et al. 2020; Tagawa et al. 2021; Wang et al. 2021).

To determine the influence of orbital eccentricity on the spin evolution of sBH populations and subsequent merger signals in detail, quantitative prescriptions for CSD flow transition should be incorporated into population synthesis models of sBH evolution in AGN disks. While Li et al. (2022) demonstrate a generic transition eccentricity e_t between prograde and retrograde CSDs dependent on companion mass ratios and disk properties, their 2D simulations do not cover sufficient parameter space to conclude a comprehensive scaling for e_t. In this Letter, we follow Bailey et al. (2021) and perform extensive 3D simulations of companion-disk interaction to determine the detailed dependence of e_t on companion mass and disk properties. The simulation setup is laid out in

Section 2, we analyze our results in Section 3 and discuss the implication of our concluded e_t formula in Section 4.

2. Numerical Setup

We use Athena++ to solve hydrodynamic equations in a spherical coordinate system ($r_\bullet$, $\theta_\bullet$, $\phi_\bullet$) rotating at the Keplerian frequency Ω_0, following the setup of Bailey et al. (2021); for the details see Section 2. A companion of mass $M_0 = qM_\bullet$ with semimajor axis a and eccentricity e is set to orbit around a host mass $M_\bullet$, where q is the mass ratio. Therefore, the location of the companion embedded in the midplane ($r_\bullet$, $\theta_\bullet = \pi/2$, $\phi_\bullet$) is described with the epicyclic approximation:

$$\begin{aligned} r_\bullet &= a(1 - e\sin\Omega_0 t) \\ \phi_\bullet &= -2e\cos\Omega_0 t. \end{aligned} \tag{1}$$

The code unit system is $G = M_\bullet = a = 1 = \Omega_0$. The sound speed is a fixed value $c_s = h_0 v_{K,0}$ such that the disk is globally isothermal, where $v_{K,0} = \Omega_0 a = 1$ is the Keplerian velocity of the guiding center and h_0 is the aspect ratio at $r_\bullet = a$. The aspect ratio h and the disk scale height $H = hr_\bullet$ are functions of distance

$$h = h_0(r_\bullet/a)^{1/2},\ H = h_0 a(r_\bullet/a)^{3/2} = H_0(r_\bullet/a)^{3/2}, \tag{2}$$

but within a small radial range centered at $r_\bullet$, they are going to be very close to h_0, H_0. We explore a range of $h_0 = 0.01$, 0.03, 0.05 in our simulations. The initial axisymmetric hydrostatic equilibrium profile is set up according to Bailey et al. (2021), which gives roughly a power-law radial distribution for the midplane density $\rho(\theta_\bullet = \pi/2) \approx \rho_0 r_\bullet^{-3}$, and a vertically integrated surface density $\Sigma \propto r_\bullet^{-3/2}$. A fiducial $\rho_0 = 1.0$ was chosen but only acts as a normalization constant since we do not include active self-gravity or gas feedback on the companion. The companion potential term was increased gradually over two orbits ("ramped up") to the designated value.

We define the following relevant length scales to facilitate our analysis. The Bondi radius

$$R_B = \frac{GM_0}{c_s^2} = \frac{q}{h_0^2}a \tag{3}$$

arises as the natural length scale comparing the companion gravity to the thermal state of the nebular gas. The Hill radius

$$R_H = \left(\frac{M_0}{3M_\bullet}\right)^{1/3} a = \left(\frac{q}{3}\right)^{1/3} a, \tag{4}$$

on the other hand, is the natural length scale comparing the strength of companion gravity with the host's tidal gravity in the corotating frame.

The thermal mass ratio is defined as

$$q_t = \frac{q}{h_0^3} = \frac{R_B}{H_0} = \frac{\sqrt{3}}{3}\left(\frac{R_B}{R_H}\right)^{3/2}. \tag{5}$$

Such that low-mass companions lie in the subthermal regime where $R_B \lesssim R_H \lesssim H_0$, represented by $q_t \lesssim 1$; moderate-mass companions lie in the superthermal regime, where $H_0 \lesssim R_H \lesssim R_B$, represented by $q_t > 1$. Additionally, considering the companion's extra epicyclic velocity about its guiding center $ev_{K,0}$, the effective Bondi radius is reduced to the Bondi–Hoyle–Lyttleton radius

$$R_{\rm BHL} = \frac{GM_0}{c_s^2 + (ev_{K,0})^2} = \frac{q}{h_0^2 + e^2}a, \tag{6}$$

which depicts more accurately an impact parameter of the circumcompanion disk (hereafter generally referred to as a CSD) in either all subthermal cases or superthermal cases where e is sufficiently large. The softening scale of $\epsilon = 0.03\ R_B$ for companion potential is deliberately chosen to resolve CSD flow patterns for a companion that has sufficiently small physical/atmospheric radius compared to R_B, most applicable to sBHs. This softening is also much smaller than the Hills radius, even for our largest superthermal companions ($q_t \leqslant 7$, such that R_H/R_B is no smaller than 0.15). We also restrict our simulations to $e < 4h_0$ to ensure $\epsilon < R_{\rm BHL}$ in superthermal cases even if $R_{\rm BHL} < R_H < R_B$. We also constrain the absolute eccentricity to be $e \lesssim 0.15$, beyond which the companion finds it hard to maintain such eccentricity long-term and the epicycle approximation may be inaccurate. All models are run for 40 orbits, which is enough time for flow fields to reach a quasi-steady or quasiperiodic state.

2.1. Boundaries and Resolution

Identical to Bailey et al. (2021), we cover the computational domain $r_\bullet \in [3a/5,\ 5a/3]$, $\theta_\bullet \in [\pi/2,\ \pi/2 + 0.2]$, and $\phi_\bullet \in [0,\ 2\pi]$ with a root grid of $64 \times 16 \times 512$, such that the root cell around $r_\bullet = a$ has a width of $\Delta \sim 0.01$. The azimuthal and polar spacings are linear and the radial spacing is logarithmic. We also apply fixed radial boundaries, periodic azimuthal boundaries, and reflecting polar boundaries.

To properly resolve the CSD region, we apply adaptive mesh refinement and impose maximum-resolution over a whole volume within a distance of $0.006a = 20\epsilon(R_B/0.01a)^{-1} = 20\epsilon q_t^{-1}(h_0/0.01)^{-1}$ from the companion location. This distance ranges from two softening lengths for the largest q_t, h_0 to 40 softening lengths for the smallest choice of q_t, h_0. Within this region of maximum-resolution, we add seven layers of refinement on top of the root grid such that for the smallest cell width $\Delta/2^7 < \epsilon$ is guaranteed for $R_B > 0.005a$, and the smoothing length can be resolved. Away from the companion, the resolution adjusts itself to relax gradually outside the region of maximum-resolution toward the default background resolution.

3. Results

3.1. Fiducial Cases

Since we apply lower central resolution and larger softening than the $\epsilon = 0.015\ R_B$ simulations in Bailey et al. (2021), we are able to run each simulation much quicker. For each given companion mass ratio q and characteristic scale height h_0, we are able to sample a number of eccentricities to determine the transition point to high accuracy. For example, it is reported in Bailey et al. (2021) that for $q_t = 0.25$, $h_p = 0.05$ ($q = 3.125 \times 10^{-5}$), the CSD flow should be prograde for $e \lesssim 0.05$ but retrograde for $e \gtrsim 0.075$, while we are able to identify $e_t = 0.066 \pm 0.001$ for a similar parameter $q_t = 0.2$, $h_p = 0.05$ ($q = 2.5 \times 10^{-5}$). Such a mass ratio is applicable to Neptunes around solar-mass planets or sBHs around low-mass $\sim 10^6\ M_\odot$ SMBHs.

We plot in Figure 1 the midplane specific angular momentum with respect to the companion J_0 for the marginal

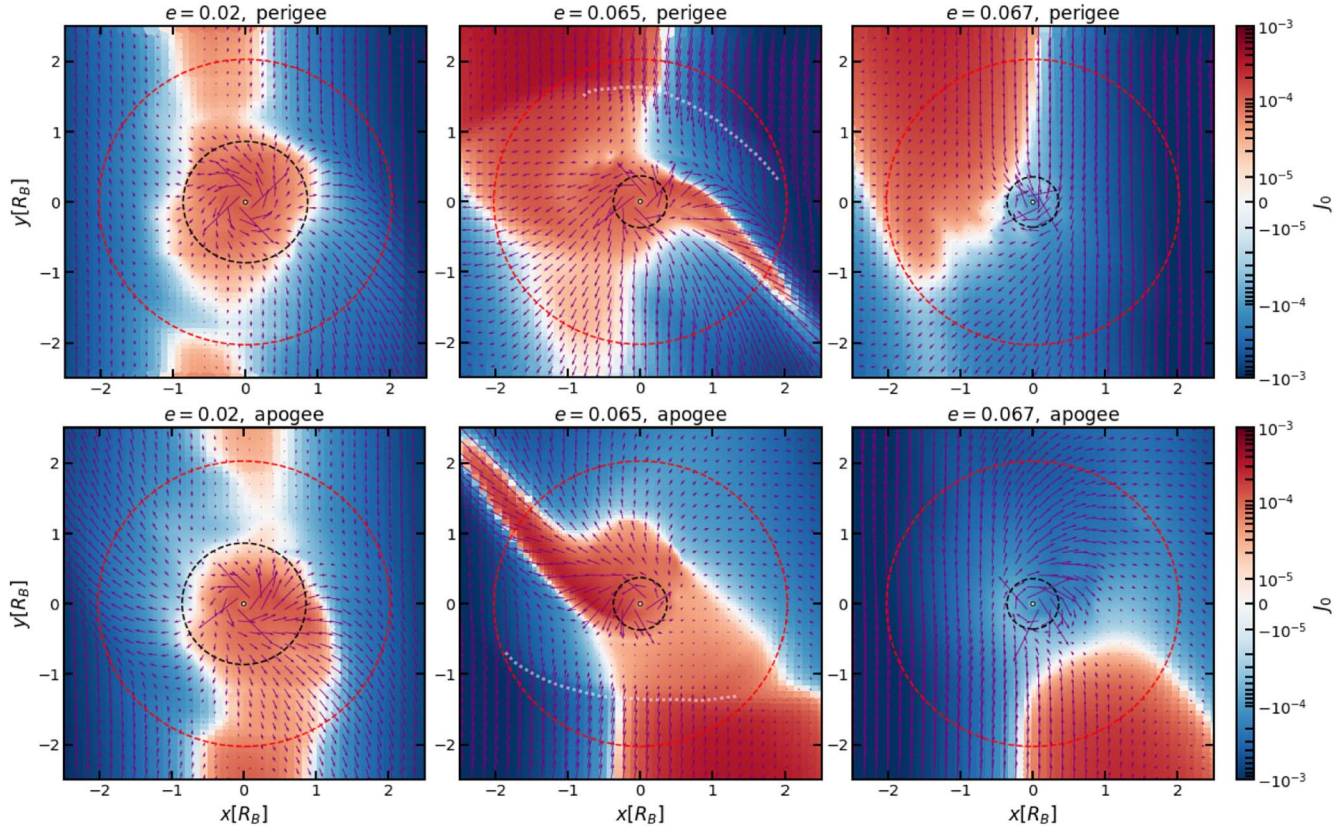

Figure 1. Flow pattern around the embedded companion. The color shows the specific angular momentum of gas J_0 relative to the companion (red: prograde; blue: retrograde), and the purple arrows represent the flow velocity around the companion. The three columns correspond to $e = 0.02$, 0.065, 0.067 cases for parameters $h_0 = 0.05$ and $q_t = 0.2$. Upper/lower panels are at the apogee/pergee. The flow quantities are averaged over the last 10 snapshots at the companion's perigee/apogee passing. The innermost solid black circle is the softening length ϵ, the black dashed circles represent $R_{\rm BHL}$, while the red dashed circles represent R_H. The x, y coordinates are normalized in R_B. The faint white dashed lines roughly indicate shock fronts.

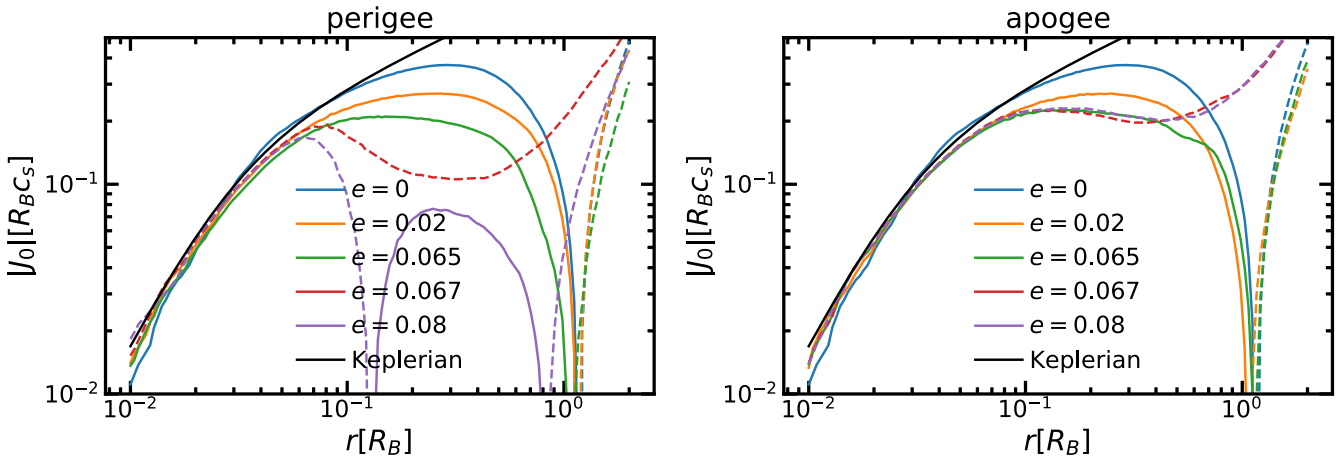

Figure 2. Azimuthally averaged J_0 profiles around the embedded companion. The companion-centric distance r is plotted in logarithmic scale to offer a closer-in scrutiny compared to Figure 1. Different colors correspond to different orbital eccentricities. Solid lines plot positive (prograde) rotation whereas dashed lines plot negative (retrograde) rotation. Keplerian profiles are shown for comparison in black holes, which deviate from power laws at small r due to gravitational softening. Left/right panels show the profiles at the perigee/apogee.

cases $e = 0.065$ (prograde CSD, upper panel) and $e = 0.067$ (retrograde CSD, lower panel), analogous to Figure 2 of Li et al. (2022). The left panels are at perigee and right panels are at apogee. As in Bailey et al. (2021), we make use of another unsubscripted coordinate system (x, y, z) or (r, θ, ϕ) centered on the *companion* to discuss the rotational aspect of the CSD flow. In this coordinate system, J_0 is the product of companion-centric distance r, and the gas velocity component along the companion-centric azimuth v_ϕ. The red color is prograde motion and blue is retrograde. The distances in Figure 1 are measured in R_B and the central solid black circles denote $\epsilon \ll R_B$. Additionally, we plot R_{BHL} with a black dashed circle and R_H with red dashed circles. At large radial locations from the companion, the Keplerian shear background is always retrograde. Within $R_{\rm BHL} \lesssim R_B$, gas is subject to the companion's gravity and its rotation always forms a CSD, regardless

of the sign of the specific angular momentum. We plot in Figure 2 the ϕ-averaged J_0 distribution (in other words, rotation curves) up to a much smaller scale within R_B compared to Figure 1, which confirms that at both perigee and apogee, the prograde/retrograde rotations converge to Keplerian at small enough radii. The Keplerian rotation deviates slightly from a power law at small r due to the prescribed gravitational softening. For increasing eccentricity, the convergence toward axisymmetric Keplerian flow (or toward a CSD structure) happens at smaller radii since realistic impact parameter R_{BHL} continues to decrease. The rotation curves at other orbital phases show similar results.

We can compare our fiducial results with 2D simulations in Li et al. (2022) for a similar parameter $q = 3 \times 10^{-5}$ and $h_0 = 0.05$. Our transition eccentricity is significantly larger than their value around 0.02, and the morphology of flow pattern is notably different. In Li et al. (2022) (see their Section 3.1), the CSD's transition from classical prograde to retrograde is directly associated with the receding of horseshoe structures from the CSD region at $e \gtrsim 0.02$, above which the CSD flow becomes directly connected with retrograde background. For even larger supersonic eccentricity $e \gtrsim 0.05$, a strong prograde headwind region appears at the upper left/lower right corner of the planet at perigee/apogee adjacent to the retrograde CSD, a feature of the shear background flow due to orbital eccentricity, which penetrates deeper into R_B and introduces more fluctuations in the CSD rotation curve as e continues to increase.

While our result for retrograde CSDs at $e > e_t$ is similar to the 2D high eccentricity limit (e.g., $e = 0.067$), prograde CSDs in 3D formed through tidal interaction seem to be much more resilient to disturbances, such that it could still preserve its rotation for eccentricities up to e $\gtrsim h_0$ even when the classical horseshoe flow pattern has been disrupted. Indeed, even in the limit of negligible eccentricity, a major feature of 3D circumcompanion flow structure compared to 2D is that the horseshoe region is narrower and the radial velocity of gas making U-turn is much smaller, as shown in Figure 3 of Ormel et al. (2015b). This is why even for small eccentricity $e = 0.02$ (left panel, Figure 1), the red band with prograde motion at large azimuths from the planet, representing horseshoe streamlines with notable radial motion, is quite narrow compared to 2D simulations.

Despite having a more significantly prograde horseshoe region at low e, above $e \sim 0.02$ the CSD turns abruptly from prograde to retrograde in 2D. However in 3D, we found that the flow pattern similar to the $e = 0.02$ case can be maintained up to e $\sim h_0$. At even larger eccentricity, the classical horseshoe structure becomes completely replaced by the aforementioned headwind region, e.g., in the marginally prograde case $e = 0.065$ (middle panel, Figure 1). Due to the supersonic epicyclic velocity, a shock front (sketched out with faint white lines) appears and barricades a prograde CSD against the disk background, which it continuously rams into. For even larger $e = 0.067$ (right panel, Figure 1), the shock front finally breaks down and the background overcomes the CSD to mold it into a retrograde flow.

To summarize different eccentricity regimes, at e $\lesssim h_0$ the CSD is mildly perturbed and shows signs of detaching from a horseshoe region that is narrower compared to 2D simulations; at $h_0 \lesssim e \lesssim e_t$ the horseshoe flow pattern disappears, while a shock front appears between the CSD and the background disk, but the prograde rotation is still maintained. At $e \gtrsim e_t$ the CSD becomes retrograde where the midplane flow pattern is similar to 2D retrograde cases.

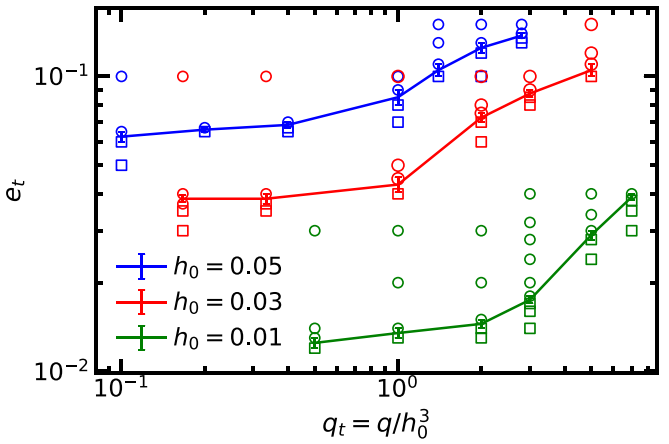

Figure 3. Simulation results from the parameter survey. For each q_t (horizontal axis) and h_0 (color), we vary eccentricity (vertical axis) and locate the transition eccentricity as a function of e_t (solid lines with error bars) to be between the largest e for prograde CSD rotation outcome (squares) and the smallest e for retrograde CSD rotation outcome (circles).

Apart from the appearance of the parameter space $h_0 \lesssim e \lesssim e_t$ where companions could maintain prograde CSDs for slightly supersonic eccentricities, the generic transition to retrograde in 2D and 3D is qualitatively similar. Namely, the CSD flow changes from tidal effect dominated to shear background dominated at large e, albeit in 3D, the transition is better marked by the fading of a shock front rather than horseshoe patterns. Our finding implies that the retrograde criterion is connected to the ability of background retrograde flow to penetrate into the shock fronts (observed in prograde cases) and to overcome the CSD. We try to directly associate this with the size of CSDs in Section 3.2.

3.2. The Parameter Survey

After running resolution convergence tests with $\epsilon = 0.015\, R_B$ and an extra layer of central refinement for the fiducial case (resolution of Bailey et al. 2021), we found an identical result $e_t \sim 0.066 \pm 0.001$, with flow patterns that are the same as Section 3.1 for $e = 0.065$ and $e = 0.067$. We conclude that it is adequate to apply our default resolution for large parameter surveys. In our full survey, we cover three scale heights $h_0 = 0.01$, 0.03, 0.05, and extend to larger q_t. The low scale height especially applies to AGN disks (Sirko & Goodman 2003; Levin 2007). The companion mass can be scaled to planetary/SBH masses of

$$M_0 = \begin{cases} 40 M_\oplus q_t \left(\frac{h_0}{0.05}\right)^3 \frac{M_\star}{M_\odot} \text{ in PPDs} \\ 100 M_\odot q_t \left(\frac{h_0}{0.01}\right)^3 \frac{M_\star}{10^8 M_\odot} \text{ in AGN disks.} \end{cases} \quad (7)$$

We summarize the results of our survey in Figure 3. The transition eccentricity e_t (with error bars) is plotted against q_t in solid lines. Different colors correspond to different h_0, and each column of symbols represents a set of simulations with fixed (h_0, q_t) but varying e: the squares represent prograde final states for the CSDs at $e < e_t$ while circles represent prograde ones at $e > e_t$.

We start from $R_B/a = 0.005$ ($q_t = 0.005/h_0$) where the softening length $\epsilon = 1.5 \times 10^{-4} a$ is narrowly resolved by $\sim$9

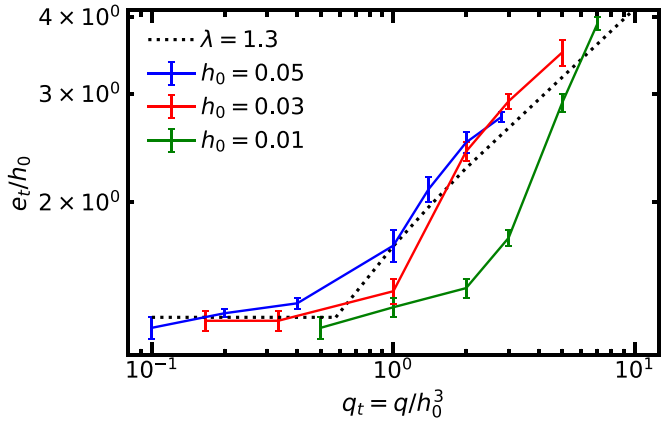

Figure 4. Similar to Figure 3, only the e_t scalings are normalized by h_0. Dotted black line shows the analytical prescription from Equation (12) with parameter $\lambda = 1.3$.

cells, then we simulate progressively larger q_t cases at each h_0. For subthermal companions with $q_t \lesssim 1$, we found a generic $e_t \sim h_0$ insensitive to q_t, as hypothesized by Bailey et al. (2021) (supersonic eccentric velocity leads to retrograde flow). However, for superthermal companions with $q_t \gtrsim 1$, the e_t scaling steepens. This dependence of e_t on the companion mass is quite significant for our largest masses at $q_t \sim \mathcal{O}(1)$.

A natural way to account for the steepening of the scaling is to interpret the supersonic eccentricity retrograde flow criterion $e \gtrsim \lambda h_0$ as a requirement for the size of Bondi-Hoyle-Lyttleton (BHL) radius with respect to the circular-orbit impact parameter, e.g., the Bondi radius in the subthermal limit:

$$(1 + \lambda^2) R_{\rm BHL} \lesssim R_B, \tag{8}$$

which means that when eccentricity is large and the epicyclic headwind is strong enough, R_{BHL} will be small enough, such that the CSD's characteristic bounded angular momentum can no longer maintain a shock front and it becomes significantly perturbed by the background retrograde flow, as discussed in Section 3.1.

To generalize to superthermal companions, we express the reference impact parameter by $\min[R_B, R_H]$ and obtain

$$(1 + \lambda^2) R_{\rm BHL} \lesssim \min[R_B, R_H], \tag{9}$$

which translates into

$$\sqrt{e^2 + h_0^2} \gtrsim \sqrt{1 + \lambda^2}\, \max[h, 3^{1/6} q^{1/3}], \tag{10}$$

so the transition eccentricity can be expressed as

$$\sqrt{1 + (e_t/h_0)^2} = \sqrt{1 + \lambda^2}\, \max[1, 3^{1/6} q_t^{1/3}] \tag{11}$$

or explicitly

$$e_t = h_0 \sqrt{(1 + \lambda^2) \max[1, 3^{1/3} q_t^{2/3}] - 1}\,. \tag{12}$$

This formula for the retrograde criterion naturally gives us a transition of scaling from $e_t \gtrsim \lambda h_0$ toward $e_t \gtrsim \lambda q_t^{1/3} h_0$ at $q_t \gtrsim 1$. Note that $\lambda > 0$ implies that $R_{\rm BHL} < R_H$ always holds at $e \geqslant e_t$ even for superthermal companions.

In Figure 4 we plot the normalized eccentricity e_t/h_0 against q_t for all our h_0 and compare them with Equation (12), assuming $\lambda = 1.3$. This λ is chosen to fit with the flat e_t scaling on the subthermal $q_t < 1$ side, which appears to be quite universal for all values of h_0; the superthermal $q_t > 1$ side of our analytical scaling fits quite well with $h_0 = 0.05$, 0.03 cases. The e_t scaling produced in our $h_0 = 0.01$ simulation starts to rise from the flat profile only after $q_t \gtrsim 3$ but also quickly catches up toward $q_t^{1/3}$ scaling afterwards, possibly because shocks are stronger for low sound speed in a nonlinear way and a prograde CSD is more easily overcome by shock for certain companion masses.

It is possible that the $q_t^{1/3}$ scaling might break down for an even larger mass regime, which is beyond the scope of this study. Nevertheless, we note that if we extend this scaling to binaries of comparable mass $q \sim 1$, the critical eccentricity would reach order-unity, consistent with circumbinary simulations (e.g., Munoz et al. 2019; D'Orazio & Duffell 2021), in which circumsingle disks around binary components should always be prograde for arbitrary eccentricity.

3.3. Effect of Viscosity: Application to AGN Context

Albeit both simulations and observations suggest that planet-forming midplanes of PPDs have low turbulent viscosities (Bai & Stone 2013; Flaherty et al. 2017, 2020), AGN disks can be highly turbulent with magnetorotational instability (MRI; Balbus & Hawley 1998) and gravitational instability (GI; Gammie 2001) providing effective turbulence parameter α (Shakura & Sunyaev 1973) up to $\sim 10^{-3}$–10^{-1} (Goodman 2003). To briefly explore how turbulent viscosity affects inviscid flow structures, we run additional tests based on the $h_0 = 0.01$, $q_t = 1$ model (corresponding to $M_0 = 100\, M_\odot (M_\bullet/10^8\, M_\odot)$ in an AGN context) focusing on determining the transition eccentricities around e_t, with constant kinetic viscosity $\nu = 4 \times 10^{-7}$ in code units to approximate a turbulence parameter $\alpha \approx \nu/c_s H_0 = 0.004$ close to the companion. We found that with a moderate viscosity, e_t is reduced slightly to 0.0125 ± 0.005 from 0.0135 ± 0.005. The J_0 distributions within R_B for these marginal cases with $e \approx e_t$ are presented in Figure 5. They are all averaged over 10 perigees and the apogee distribution is quite analogous.

In the inviscid simulations (upper panels, Figure 5), the $e = 0.012$ and $e = 0.013$ flow pattern is similar to to the fiducial case at $e = 0.065$. Although $q_t = 1.0$ is slightly superthermal in the sense that $R_H \lesssim R_B$ and that in the circular-orbit limit case the CSD size should be constrained by R_H instead of R_B (Martin & Lubow 2011); from the summary in Section 3.2 we know that at around $e \gtrsim e_t$ we always have $R_{\rm BHL} \lesssim R_H$, therefore the extent of CSD rotation is still mainly constrained by the BHL radius rather than R_H. The marginally retrograde CSD structure at $e = 0.014$ is also similar to the fiducial case at $e = 0.067$ accompanied with the fading of a shock front, albeit not as abrupt as in Figure 1. The shock completely disappears around $e \sim 0.16$ closer to the e_t given by Equation (12), which may be relevant to deviation of the $h_0 = 0.01$ curve in Figure 4 from analytical prescription, in the sense that while Equation (12) can indeed reflect the point where the shock front is overcome by strong headwind, for small h_0 the CSD rotation can become dominated by background flow before the complete disappearance of the shock.

In the $\alpha = 0.004$ simulations (lower panels, Figure 5) the transition is quite similar, with $e = 0.012$ producing prograde and both $e = 0.013$ and 0.014 producing retrograde CSDs. The slight reduction of e_t is probably due to shock fronts being harder to maintain in the presence of viscosity.

Based on this additional set of simulations, we conclude that e_t is not sensitive to viscosity up to moderate values of α, and the main cause for e_t being generally much larger than Li et al.

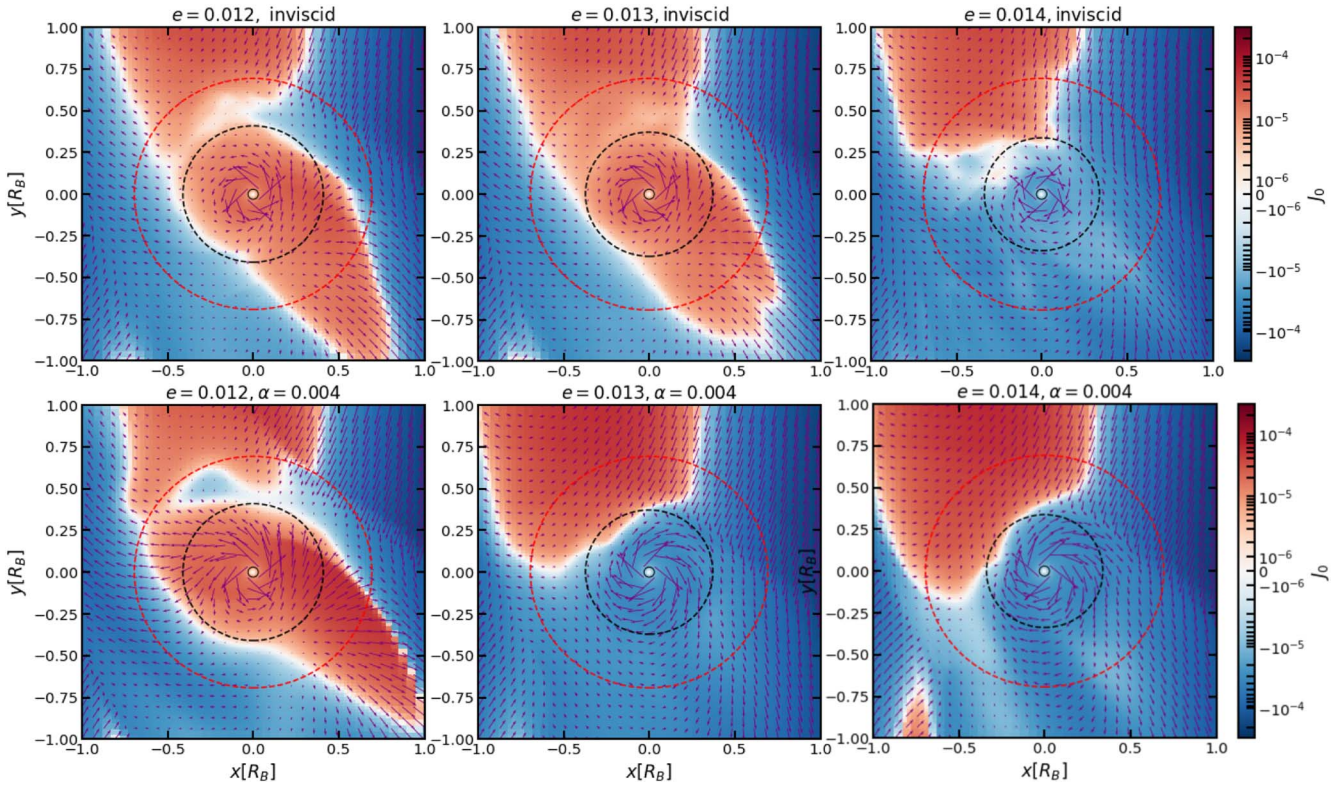

Figure 5. Flow pattern around the embedded companion similar to Figure 1. The three columns correspond to $e = 0.012, 0.013, 0.014$ cases for parameters $h_0 = 0.01$ and $q_t = 1.0$. Upper/lower panels are for inviscid/viscous simulations. The flow quantities are averaged over the last 10 snapshots at the companion's perigee passing. The results for apogee are similar and quite centrosymmetric.

(2022) should be due to 2D/3D geometry, instead of their simulations having $\alpha \sim 10^{-3}$. Nevertheless, the kinematic viscosity term $\nu = \alpha c_s H_0$ in laminar fluid equations is only to approximate the vortensity diffusion and angular momentum transfer effect of realistic turbulence (Baruteau & Lin 2010), which is useful for a low turbulence level but could fail to capture important effects from velocity/density fluctuations in the case of strong turbulence with $\alpha \sim 10^{-2}$–10^{-1}. Furthermore, magnetic fields may provide large scale coupling between the CSDs and the background flow, leading to different results from α disks (Zhu et al. 2013). To explore such levels of turbulence, it is worth performing simulations of companions embedded in realistic MRI or GI environments.

4. Conclusions

We confirm the retrograde circumstellar flow criterion for eccentric subthermal disk-embedded companions proposed in Bailey et al. (2021) and Li et al. (2022), and extend it to superthermal companions. The dependence of transition eccentricity e_t on mass ratio q and disk scale height h_0 can be incorporated into the empirical formula in Equation (12), for which we have offered some analytical understanding. Our results also suggest that e_t is relatively insensitive to viscosity. The results have several implications.

In terms of CPDs, retrograde rotation may lead to in situ formation of retrograde satellites, as an alternative channel from dynamical capture, e.g., the case of Triton (McKinnon & Leith 1995). Dynamical events such as mergers and ejections in multiple planets can excite eccentricity of planets to typically $\gtrsim$0.1 (Zhou et al. 2007; Ida & Lin 2010; Ida et al. 2013; Bitsch et al. 2020). In the presence of a gaseous disk, large eccentricities are quickly damped toward a residual value $\sim h$ if low-mass planets form mean-motion resonance chains through migration (Zhang et al. 2014; Liu et al. 2015). Therefore, it is still likely that moderate eccentricity and retrograde CPDs could be maintained for a considerable fraction of PPD lifetimes, which is adequate for significant in situ pebble growth in CPDs (Drażkowska & Szulágyi 2018; Szulagyi et al. 2018). Considering $h_0 \approx 0.05$ in PPDs similar to the early outer solar nebula (Chiang & Youdin 2010), $q_t \approx 8$ for Jupiter mass, and $q_t \approx 2$ for Saturn mass so their e_t is large. Therefore it may be more likely to form retrograde CPDs around subthermal, Neptune-mass objects. Subsequent works may explore solid accretion in retrograde CPDs, but we generally remark that in situ formation of retrograde satellites should prefer multiplanet systems where planetary eccentricities are easier to maintain, and may be more likely around Neptune-mass planets.

For sBHs embedded in an AGN scenario, the disk scale height is typically $h_0 \sim 0.01$ (Sirko & Goodman 2003; Nayakshin & Cuadra 2007; Levin 2007); therefore the normalized mass ratio is nearly always subthermal ($q_t < 1$) for sBH mass $\lesssim 100\ M_\odot$, and SMBH mass in the range of 10^6–$10^8\ M_\odot$. Similar to the planetary context, multiple sBHs can also form resonance chains through migration and maintain $e \sim 0.01$ from their mutual dynamical interaction (Secunda et al. 2019, 2020). If their spin evolution is coupled with the rotation of their surrounding CSDs, the sBHs will be spin up to critical rotation on their Eddington mass accretion timescales, with circular ones being spun up in the prograde direction, and eccentric $e > e_t \sim 0.01$ ones being spun up in the retrograde direction, as discussed in some detail by Li et al. (2022). This leads to formation of a population of misaligned sBHs spun up

by prograde and retrograde CSDs, depending on dispersion in their initial eccentricity distribution. Merging of misaligned pairs of sBHs would contribute to subsequent low $\chi_{\rm eff}$ GW events. Our quantitative criterion can be readily incorporated into sBH population synthesis models (Tagawa et al. 2020a, 2020b; McKernan et al. 2022) to study the detailed influence of eccentricity distribution on the GW signal properties.

Y.X.C would like to thank Douglas Lin and Ya-Ping Li for helpful discussions. We also acknowledge computational resources provided by the high-performance computer center at Princeton University, which is jointly supported by the Princeton Institute for Computational Science and Engineering (PICSciE) and the Princeton University Office of Information Technology.

ORCID iDs

Yi-Xian Chen https://orcid.org/0000-0003-3792-2888
Avery Bailey https://orcid.org/0000-0002-6940-3161
James Stone https://orcid.org/0000-0001-5603-1832
Zhaohuan Zhu https://orcid.org/0000-0003-3616-6822

References

Bai, X.-N., & Stone, J. M. 2013, ApJ, 769, 76
Bailey, A., Stone, J. M., & Fung, J. 2021, ApJ, 915, 113
Balbus, S. A., & Hawley, J. F. 1998, RvMP, 70, 1
Bartos, I., Kocsis, B., Haiman, Z., & Marka, S. 2017, ApJ, 835, 165
Baruteau, C., & Lin, D. N. C. 2010, ApJ, 709, 759
Batygin, K. 2018, AJ, 155, 178
Bavera, S. S., Fragos, T., Qin, Y., et al. 2020, A&A, 635, A97
Bitsch, B., Trifonov, T., Izidoro, A., et al. 2020, A&A, 643, A66
Chiang, E., & Youdin, A. N. 2010, AREPS, 38, 493
Davies, M. B., & Lin, D. N. C. 2020, MNRAS, 498, 3452
D'Orazio, D. J., & Duffell, P. C. 2021, ApJL, 914, L21
Drażkowska, J., & Szulágyi, J. 2018, ApJ, 866, 142
Flaherty, K., Hughes, A. M., Simon, J. B., et al. 2020, ApJ, 895, 109
Flaherty, K. M., Hughes, A. M., Rose, S. C., et al. 2017, ApJ, 843, 150
Fung, J., Artymowicz, P., & Wu, Y. 2015, ApJ, 811, 101
Gammie, C. F. 2001, ApJ, 553, 174
Gerosa, D., Berti, E., O'Shaughnessy, R., et al. 2018, PhRvD, 98, 084036
Ginzburg, S., & Chiang, E. 2020, MNRAS, 491, L34
Goodman, J. 2003, MNRAS, 339, 937
Ida, S., & Lin, D. N. C. 2010, ApJ, 719, 810
Ida, S., Lin, D. N. C., & Nagasawa, M. 2013, ApJ, 775, 42
Korycansky, D. G., & Papaloizou, J. C. B. 1996, ApJS, 105, 181
Leigh, N. W. C., Geller, A. M., McKernan, B., et al. 2018, MNRAS, 474, 5672
Levin, Y. 2007, MNRAS, 374, 515
Li, R., & Lai, D. 2022, MNRAS, 517, 1602
Li, Y.-P., Chen, Y.-X., Lin, D. N. C., & Wang, Z. 2022, ApJL, 928, L1
Li, Y.-P., Chen, Y.-X., Lin, D. N. C., & Zhang, X. 2021a, ApJ, 906, 52
Li, Y.-P., Dempsey, A. M., Li, H., Li, S., & Li, J. 2022, ApJL, 928, L19
Li, Y.-P., Dempsey, A. M., Li, S., Li, H., & Li, J. 2021b, ApJ, 911, 124
Liu, B., Zhang, X., Lin, D. N. C., & Aarseth, S. J. 2015, ApJ, 798, 62
Lousto, C. O., Zlochower, Y., Dotti, M., & Volonteri, M. 2012, PhRvD, 85, 084015
Lubow, S. H., Seibert, M., & Artymowicz, P. 1999, ApJ, 526, 1001
Machida, M. N., Kokubo, E., Inutsuka, S.-i., & Matsumoto, T. 2008, ApJ, 685, 1220
Maeda, N., Ohtsuki, K., Tanigawa, T., Machida, M. N., & Suetsugu, R. 2022, ApJ, 935, 56
Martin, R. G., & Lubow, S. H. 2011, MNRAS, 413, 1447
McKernan, B., Ford, K. E. S., Callister, T., et al. 2022, MNRAS, 514, 3886
McKernan, B., Ford, K. E. S., Kocsis, B., Lyra, W., & Winter, L. M. 2014, MNRAS, 441, 900
McKernan, B., Ford, K. E. S., Lyra, W., & Perets, H. B. 2012, MNRAS, 425, 460
McKinnon, W. B., & Leith, A. C. 1995, Icar, 118, 392
Munoz, D. J., Miranda, R., & Lai, D. 2019, ApJ, 871, 84
Nayakshin, S., & Cuadra, J. 2007, A&A, 465, 119
Ormel, C. W. 2013, MNRAS, 428, 3526
Ormel, C. W., Kuiper, R., & Shi, J.-M. 2015a, MNRAS, 446, 1026
Ormel, C. W., Shi, J.-M., & Kuiper, R. 2015b, MNRAS, 447, 3512
Secunda, A., Bellovary, J., Low, M.-M.-M., et al. 2019, ApJ, 878, 85
Secunda, A., Bellovary, J., Mac Low, M.-M., et al. 2020, ApJ, 903, 133
Shakura, N. I., & Sunyaev, R. A. 1973, A&A, 500, 33
Sirko, E., & Goodman, J. 2003, MNRAS, 341, 501
Stone, N. C., Metzger, B. D., & Haiman, Z. 2017, MNRAS, 464, 946
Szulagyi, J., Binkert, F., & Surville, C. 2022, ApJ, 924, 1
Szulagyi, J., Cilibrasi, M., & Mayer, L. 2018, ApJL, 868, L13
Szulagyi, J., Morbidelli, A., Crida, A., & Masset, F. 2014, ApJ, 782, 65
Tagawa, H., Haiman, Z., Bartos, I., & Kocsis, B. 2020a, ApJ, 899, 26
Tagawa, H., Haiman, Z., Bartos, I., Kocsis, B., & Omukai, K. 2021, MNRAS, 507, 3362
Tagawa, H., Haiman, Z., & Kocsis, B. 2020b, ApJ, 898, 25
Tanigawa, T., Ohtsuki, K., & Machida, M. N. 2012, ApJ, 747, 47
Tanigawa, T., & Watanabe, S.-i. 2002, ApJ, 580, 506
The LIGO Scientific Collaborationthe Virgo Collaborationthe KAGRA Collaboration, et al. 2021, arXiv:2111.03606
Wang, Y.-H., McKernan, B., Ford, S., et al. 2021, ApJL, 923, L23
Zhang, X., Liu, B., Lin, D. N. C., & Li, H. 2014, ApJ, 797, 20
Zhou, J.-L., Lin, D. N. C., & Sun, Y.-S. 2007, ApJ, 666, 423
Zhu, Z., Stone, J. M., & Rafikov, R. R. 2013, ApJ, 768, 143